A MULTI-SCALE APPROACH TO A GREATER UNDERSTANDING OF THE BEHAVIOR OF HETEROGENEOUS MATERIALS UNDER DYNAMIC LOADING

by

Andrew J. Van Vooren, B.S.

A Thesis submitted to the Faculty of the Graduate School,

Marquette University.

in Partial Fulfillment of the Requirements for

the Degree of Master of Science

Milwaukee, Wisconsin

August 2013

ABSTRACT

A MULTI-SCALE APPROACH TO A GREATER UNDERSTANDING OF THE BEHAVIOR OF HETEROGENEOUS MATERIALS UNDER DYNAMIC LOADING

Andrew J. Van Vooren, B.S.

Marquette University, 2013

The penetration of granular materials is of interest to a variety of different fields, and is an active area of research. The objective of this project is to gain understanding of the dynamics of a projectile penetrating into a granular material. To do this, experiments were run and a numerical model was created.

A dart gun was used to accelerate an aluminum dart to velocities around 100 m/s, which then impacted a target tank filled with Ottawa sand. The dart flew along a view window, which allowed for a recording of the penetration event using a high speed camera. Pressure gauges inserted into the target tank measured the timing and magnitude of the compaction wave created by the dart. In these penetration events a two wave structure was discovered; a compaction wave and a fracture wave. The damage wave is characterized by a white cone around the nose of the dart, which is created by increased reflectance from the newly created fracture surfaces in the grains of sand.

An experiment was conducted in which single grain of sand was crushed. From this experiment it was discovered that the phenomenon that creates increased reflectivity is the creation of fractures faces in the sand, and is not triboluminescence. Stress-strain data for the sand was also gathered, to be used in the numerical simulation. An ultrasonic pulser/receiver was used to gather data on the longitudinal and shear wave speeds through “as poured” Ottawa sand; 263 m/s and 209 m/s respectively. It was determined that the compaction and damage wave speeds were not related to either the longitudinal or shear wave speeds.

A numerical model was created using an EMU Peridynamic code. This code utilizes integral rather than differential equations, which allows for the modeling of crack propagation and fracture. The numerical simulations run were two-dimensional and on a smaller scale than the penetration experiments. The numerical simulation showed evidence of a compaction wave, force chain creation, and grain fracture, all of which were also observed in the penetration experiments.

ACKNOWLEDGEMENTS

Andrew J. Van Vooren, B.S.

TABLE OF CONTENTS

LIST OF TABLES

LIST OF FIGURES

CHAPTER 1. INTRODUCTION

1.1. Background of the Penetration of Granular Materials

The penetration of granular materials is of interest to a variety of different fields, and is an active area of research. Granular materials are of interest to groups interested in the ballistic penetration of soils (sand, dirt, etc.), planetary impacts, etc. The reaction of granular materials being impacted in many different regimes has been studied. Under certain circumstances, granular materials can interact like a liquid, a solid, or separate from both.

It is generally well understood how granular materials react to static loading. First, the sand is compacted until it enters a semi-stable configuration. Then the grains of sand form force chains, which extend deep, generally to the edges of the container the test is being done in. As the force on the material increases, certain grains begin to fracture. As these grains fracture, the granular material reorganizes into a new semi-stable configuration, creating new force chains.

1.2. Literature Review

1.2.1. Experimental Granular Penetration Literature

One of the first and most referenced studies into the penetration of sand was done in 1957 by Allen, Mayfield, and Morrison [1][2]. In their first work they investigated previous empirical formulas for the penetration of a conical nosed projectile through sand. They also found evidence for a critical velocity, which they found to be approximately 100 m/s. They believe that this is the velocity at which a projectile transitions from inelastic to elastic impact, and that the critical velocity is based upon the speed of sound in the sand. In their second work released in the same year, they created more experimental setups to verify their previous equations for the penetration using the critical velocity. They also investigated whether the critical velocity was related to the speed of sound in sand as they had previously hypothesized. They found that the critical velocity was not related to the speed of sound of the material, it was neither the same velocity nor is it directly proportional.

In 1993Liu and Nagel investigated the speed of sound in sand [3]. They studied not only the velocity of sound through the sand but also other interesting characteristics such as non-linearity based on the amplitude of the waves and frequency shifts. They found that the speed of sound in their sand at a depth of 6cm is 280±30 m/s. They also believed that the nonlinearity in their data at high amplitudes occurs because of hysteresis effects. The high amplitudes create force chains in the sand, and brings into contact grains that were not previously in contact with each other, which creates this non-linear effect.

In 2001 the Institute of Problems in Electrophysics of Russian Academy of Sciences (IPE RAS) studied the configuration that created the maximum possible penetration depth of a projectile [4]. Some of the variables that they considered were projectile material, velocity of projectile (ranging from .85 to 3 km/s), and the shape and dimensions of the projectile. They found that there is a critical velocity (different from the critical velocity discovered by Allen, Mayfield and Morrison) which is the velocity at which the projectile begins to melt as it impacts the sand. This critical velocity is primarily a function of the melting temperature of the material of the projectile, and exceeding this velocity leads to lower penetration depths. The IPE RAS study also found that the most important material characteristic to determine the penetration depth is the density of the projectile, with higher densities allowing for higher penetration depths. Their final discovery is that at high velocities, projectiles with a very high L/D (length over diameter) ratio will bend or break, leading to reduced penetration depth. For maximum penetration depth they recommend a dense material with a high melting temperature, and a projectile with L/D ratio of 5-7.

In 2008, Goldman and Umbanhowar investigated sphere and disk projectiles penetrating granular materials at low velocities [5]. They were interested in parameters including penetration depth, collision duration, and deceleration of the sphere. They found that at velocities between 2 and 5 m/s, the penetration depth scaled linearly with projectile velocity. They also created a semi-empirical equation to calculate the force on the sphere based on the acceleration data that was recorded.

In 2010, Cooper and Breaux investigated the fracture characteristics of grains of sand at high velocities [6]. They shot projectiles at speeds of 600 and 1,200 m/s and sand densities of 1.55 and 1.73 g/cc. The primary concern of this research was to understand the types and extent of fracture of the grains of sand. They saw that there were significant piles of crushed grains of sand along the penetration path, evidence that some of the fractured grains became entrained behind the projectile, and fractured sand residue along the side of the projectile. They also used a SEM to gain visual evidence for fracture plains on the grains. Evidence that the amount of grains fractured increases as velocity decreases was also presented.

Goldman and Umbanhower released another paper in 2010, which focused on the effect of the volume fraction of glass spheres when impacted by steel spheres [7]. They were able to identify a critical packing state, where the volume fraction neither increases nor decreases when subjected to a shear stress. They found that previous models were able to model the penetration parameters when the volume fraction was near to the critical packing state, but no models discussed could accurately model high or low volume fractions.

In 2012 Omidvar, Iskander and Bless, created a review of the research done on the stress-strain behavior of sand [8]. They focused on data gathered using the following four methods: uniaxial compression, Split Hopkinson Pressure Bar (SHPB), triaxial compression, and plane shock wave tests. It was found that strength increases with increases confining pressure.

Data stating that the amount of grains of sand fractured decreased when undergoing high strain rate deformation as opposed to static, confirming the results presented by Cooper and Breaux.

Also in 2012, Marston, Vakarelski, and Thoroddsen investigated the penetration of wet glass beads by spheres at low velocities, 0 to 5m/s [9], similar to as has been done for dry sand [5]. They found that the depth of penetration for the wet case can either be higher or lower than that of the dry case, depending on the percent saturation. There is an increase in penetration depth at low saturation levels, which transitions to a decrease in penetration depth as the percent saturation increases. Evidence is presented that confirms that the depth of penetration decreases as the volume fraction of sand increases. They also calculated yield stress and viscosities for the saturated granular material.

The triaxial and uniaxial states of stress for dry sand were compared in 2012 by Martin, Kabir, and Chen using a SHPB [10]. They found that the strength of the sand could be increased by increasing the confining pressure. Evidence was presented that showed that under uniaxial strain the material is very sensitive to initial density, but under triaxial stress it is not sensitive to density.

1.2.2. Modeling Granular Penetration Literature

In 2004, Ciamarra et al. investigated the forces on a projectile penetrating a granular medium using a combination of an experiment and a numerical simulation. For their experiment they used stacked glass cylinders trapped between parallel plates, creating a pseudo two dimensional experiment. This experiment used slow penetration velocities (1-3 m/s) and the grains were not damaged. For this reason, they did not consider the strength of the grains in their numerical model. They found that the time it takes for the projectile to stop is independent of the velocity at impact. By plotting the magnitude of the force on each grain, they were able to demonstrate the presence of force chains in their simulations.

Borg and Vogler investigated using mesoscale simulations rather than continuum constitutive models to simulate the penetration of a granular material using hydrodynamic calculations [12]. These simulations were successful in showing that it was possible to create a mesoscale simulation which would be sensitive to grain scale variations. They added some grains that were significantly larger than the other grains, in low volume fraction amounts, and found that this has a large effect on the penetration and trajectory of the projectile. They also found that altering the fracture strength of the sand had a large effect on the penetration of the projectile. This is supported by experiments referenced in that paper which showed evidence of fine quartz powder along the trajectory of the projectile.

Dwivedi et al. used mesoscale simulations to study the stability of projectiles penetrating granular materials [13]. They considered projectiles with velocities from 500 to 1500 m/s, and grains of sand with and without friction included. They found that instability increased with increasing velocity, and that the random arrangement of grains did not impact the stability of the projectile as long as variables such as volume fraction were maintained. It was also determined that the projectile became more stable as the porosity decreased, because there was less penetration resistance. These calculations did not allow for the fracture of the grains, but damage to the projectile was considered.

In 2011, Collins et al. investigated using Digital Speckle Radiography to measure the internal flow fields of a penetration event into a granular medium, and attempted to replicate those results using numerical simulations [14]. They found that at the beginning of the penetration event there is a period where the dart begins to create a compaction wave which creates a volume of sand that moves in the direction of the projectile. This dynamic behavior creates a large deceleration as the compaction wave is being formed, but allows for reduced deceleration once a stable compaction wave has formed. They also found that a hemispherical or ogive nosed projectile will decelerate less during this compaction wave formation, leading to a higher velocity once the wave has formed. They did not mention whether or not there was evidence of grain destruction in these penetration events. Their numerical simulations showed evidence of force chain creation. The simulation had a velocity distribution similar to that of the experimental results, as long as the grains are randomly placed.

Borg et al. investigated the impact, penetration, and cavity formation during the penetration of a granular material using experiments as well as continuum simulations [15]. The high speed images gathered in this experiment showed that there was little contact between the sand and the sides of the projectile, which means that there would be small shear stress on the dart. The projectiles for this experiment remained fairly stable, both for spherical and cylindrical projectile shapes. Using particle image velocimetry, it was discovered that a majority of the momentum that was imparted into the sand was in a direction perpendicular to the projectile, which aided in the creation of a larger vertical cavity. The continuum simulations were not able to capture the velocity field imparted on the sand, although simple analytic models were capable of getting close to the depth of penetration of the projectiles. This shows that it is necessary to use something other than continuum simulations to fully model the reaction of granular materials. The spherical projectile had a constant depth of penetration over a velocity range of 130 to 215 m/s.

1.3. Purpose and Methodology

In the experiments described above, there were multiple empirical models created to predict the depth of penetration a projectile of a certain size will be capable of at a certain velocity. These empirical models can predict this depth of penetration well for certain experimental setups, but fall apart when certain variables change. The type of sand, velocity of penetration, and projectile properties all have a large effect on the depth of penetration. For this reason it is desirable to create a numerical model that is capable of incorporating all of these variables.

There have also several numerical simulations which have aimed to model the penetration of granular materials. The majority of these simulations incorporated a granular depth of only one or two projectile lengths. There also have been continuum models which do not take into account the heterogeneity of the sand, which does not allow the model to account for all the dynamic effects present in experiments. Other models did not incorporate the possibilities of grains fracturing, which, depending on the velocity of the projectile and strength of the sand, can have a very large effect on the penetration dynamics.

The purpose of this project is to create an experiment which will be able to be modeled easily using a mesoscale simulation. To do this, a light gas gun will fire a projectile into a sand target, along a view window. This will allow for high speed video of the penetration event, which will in turn allow for particle image velocimetry (PIV) to be applied. There will also be pressure gauges in the sand, which will measure the pressure wave created by the projectile. This event will be modeled using a peridynamic code, which will be able to model the fracture of the grains of sand, as well as grain on grain interactions.

CHAPTER 2. EXPERIMENTAL SETUP

2.1. Penetration Experimental Setup

In order to accelerate the dart projectiles, an air gun was used. The component diagram of the air gun can be found in Figure 2.1below.

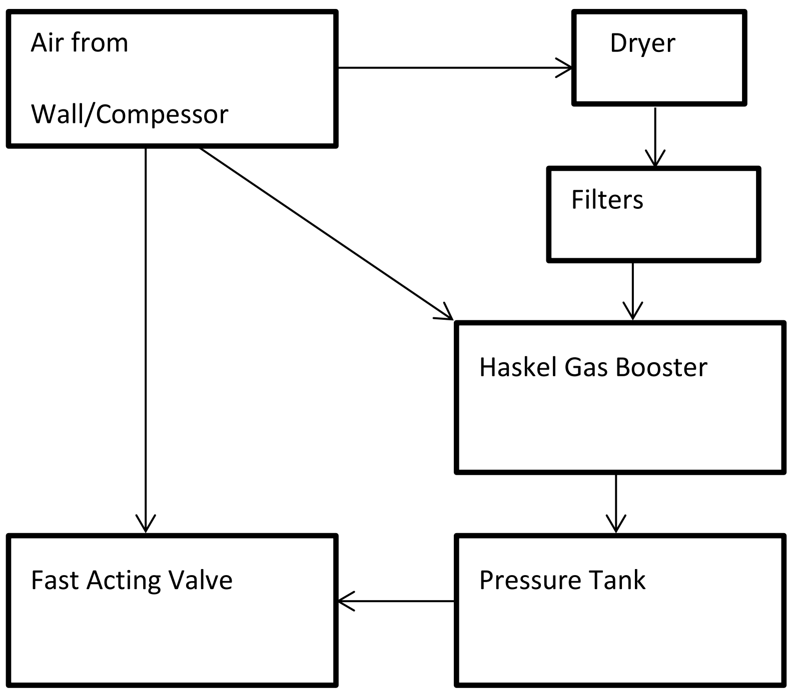

Figure 2.1. Schematic of the components of the air gun.

The air comes initially from a compressor (in our initial configuration in the Marquette University Academic Support Facility) or from the wall in our configuration (in our current Marquette University Engineering Hall configuration). Either way the air leaves this component at 100 psi and enters a dryer, to prevent condensation in later components. The air then enters a filtration system, to make sure the air going into the Haskel Gas Booster is clean. The Haskel Gas Booster uses a stream of 100 psi air directly from the compressor/wall to compress the cleaned air stream coming from the filtration stream up to pressures ranging from 300 to 900 psi. This high pressure gas is stored in the pressure tank, which creates a large reservoir of high pressure gas to use for accelerating the projectile. The fast acting valve is then able to be triggered remotely by running a current through it, and it is powered by an additional 100 psi air stream from the compressor/wall.

Once the fast acting valve is triggered, the high pressure air accelerates the dart, riding on the sabot, down the barrel. Figure 2.2 shows the projectile inserted into the sabot. The purpose of the sabot is to prevent damage to the barrel from contact with the metal projectile. The sabot has two o-rings inset in grooves in the sabot, and then is covered in vacuum grease, creating a good seal between the sabot and the barrel. The dart/sabot then reaches the end of the barrel, entering the stripper box. Inside the stripper box the dart is allowed to pass through freely, entering the target filled with sand along the view window. As the dart enters the target box, it breaks a make screen, which triggers the video camera to start filming. A circuit diagram for the make switch can be found in Figure 2.3. The sabot follows the dart into the stripper box, where it breaks the velocity pins, and is stopped in the velocity block. The times at which the velocity pins are broken is recorded on an oscilloscope. Knowing the distance between these velocity pins allows for the calculation of velocity. A circuit diagram for the velocity pin setup can be found in Figure 2.4. The sabot getting stopped here prevents high pressure air from entering the target tank and affecting the sand. Figure 2.5 shows the configuration of the barrel, stripper box, and target tank.

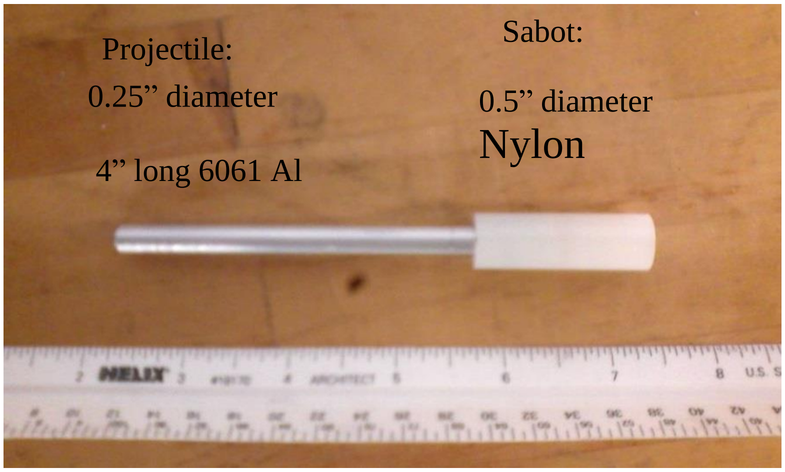

Figure 2.2. Picture of the aluminum projectile inserted into the Nylon sabot.

Figure 2.3. Circuit diagram for the camera’s make switch.

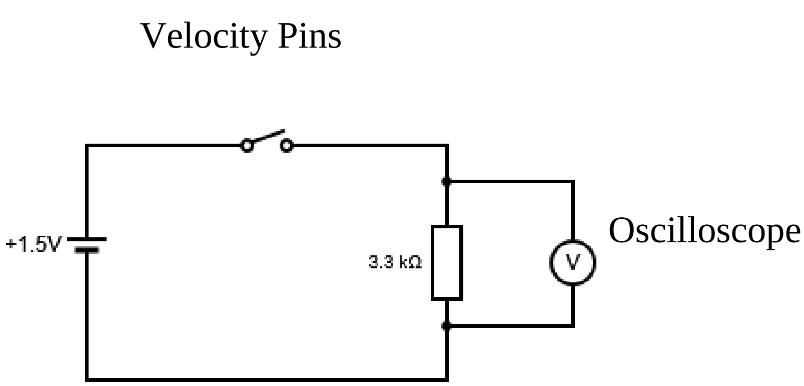

Figure 2.4. Circuit diagram for the velocity pin.

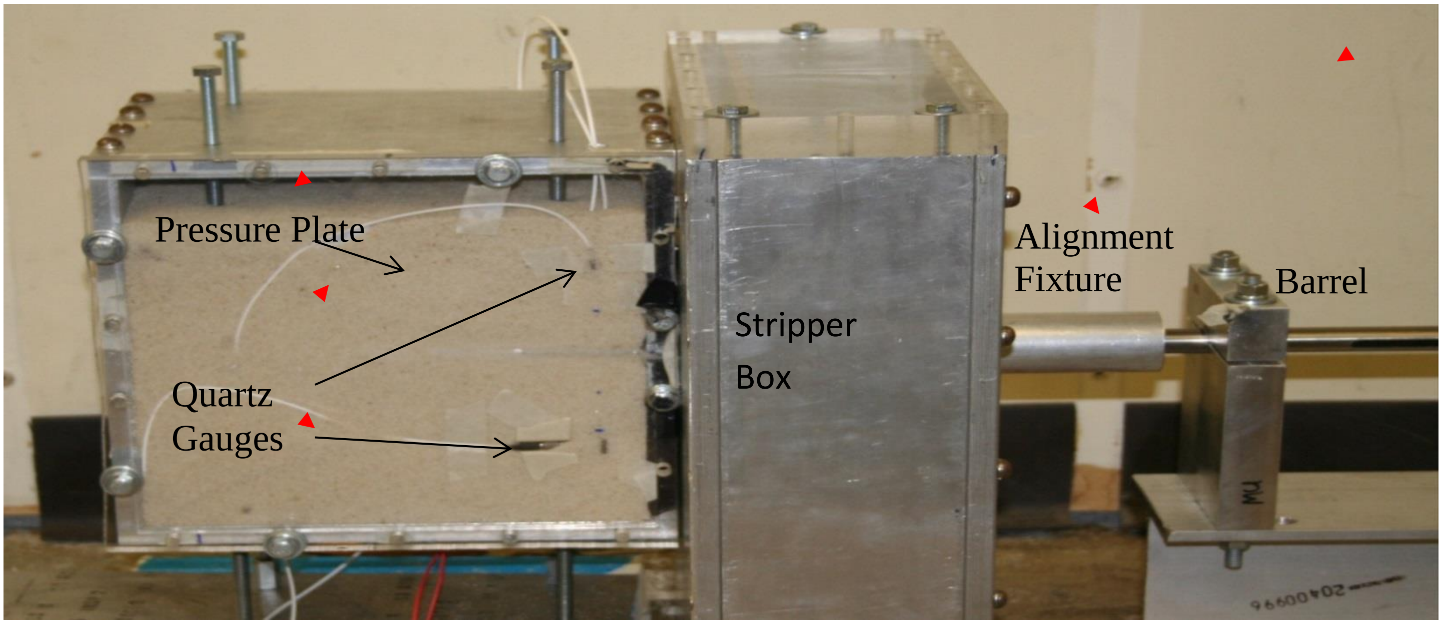

Figure 2.5. Configuration of the barrel, stripper box, and sand target box.

After the projectile enters the sand target, it flies along the viewing window. This allows us to record the penetration event with a high speed camera. A Photron APX RS camera was used to visualize the nearly the entire target box, having a field of view (fov) of 26x22cm. It was filmed at a frame rate of approximately 12,000 frames per second (fps) and a resolution of 512x432, at a shutter speed of 1/500,000 seconds. A Cordin 550 camera was used at a smaller field of view, 2.7x2.7 cm for instance, to get a close up view of the grain on grain interactions. This camera took 64 frames per event with a resolution of 1024x1024. A frame rate between 120,000 fps and 600,000 fps was used, with a shutter speed of 1/fps seconds. In order to run at such high shutter speeds, a high intensity of light was required. This was accomplished for the Photron camera using a pair of one kilowatt halogen lights, and for the Cordin 550 camera a Photogenic flash lamp was used.

Utilizing the video from the Photron camera, a velocity vector field can be attained using a matlab add-on called MPIV [16]. MPIV is a program that uses particle image velocimetry (PIV) to create a vector field. PIV works by first setting up a grid of interrogation windows. The algorithms calculate how particles in each interrogation window move by comparing two images, in our case sequential frames of the video. This system can only work if the particles travel small distance between frames, if all the particles leave the interrogation window it can no longer accurately track them. This can be partially mitigated by allowing interrogation window overlap, but it still limits the velocity that this system can measure. It also requires that the particles are of a size that they are distinguishable. It was found that a resolution of approximately 4 pixels per grain of sand worked the best. For these reasons the regions near to the dart did not give accurate velocity measurements. The Cordin 550 video had too small of a field of view to be useful for PIV.

Inside the target tank, quartz pressure gages were placed embedded in the sand, at specified distances from the shot line and target box entrance. The first pressure gauge was placed 25mm behind the target box entrance and 25 mm above the shot line. The second pressure gauge was placed at different places in the target tank depending on the experiment being done. The data from these pressure gauges gives us the pressure and arrival time of the compaction wave created in the penetration event. There is also a pressure plate inside the box. This is a steel plate toward the top of the target tank, with bolts the can be tightened to add pressure to the sand. This can be used to simulate sand at different depths, and to study how this pressure affects the penetration event.

Along with the pressure in the sand, the nose shape of the projectile was also varied. Flat, cone, and hemispherical nose shapes were all utilized in experiments. It was of interest to study how these nose shapes affected the dynamics of the penetration event, especially the relative amounts of grains fractured compared to those simply pushed out of the way of the dart. Figure 2.6 shows the different nose shapes used. The black marks on the flat nosed dart are fiducial marks, which all the darts have before being fired. These marks allow the dart to be more easily tracked once the dart is in the sand.

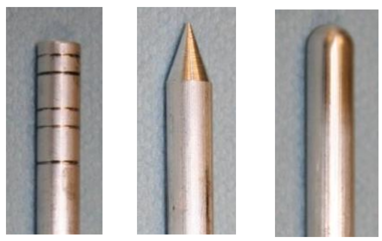

Figure 2.6. Dart nose shapes from left to right: flat, conical, hemispherical

2.2. Single Grain Experimental Setup

The motivation to do single grain experiments was twofold; to gather data on the stress/strain relationship for the particular type of sand used and to determine if the sand was displaying triboluminescence or increased reflectance due to increased faces during fracture. The stress strain data gathered from these experiments was utilized in the numerical model to make it match more closely with the experimental results. Triboluminescence is a phenomenon where a material will give of light when fractured, which can happen in certain types of quartz and other crystalline materials.

The first part of the single grain experiment aimed at determining if the grains were exhibiting triboluminescence or increased reflectivity due to the creation of fracture faces. It was also of interest to know if the phenomenon was revertible. To do this the grains of sand were placed on top of a steel plate, and were then crushed from above with another steel plate. The force stopped being applied as soon as the first sign of failure presented. This was recorded using the Photron high speed video camera. To determine if this phenomenon was the result of triboluminescence this was also done without using the 1kW halogen light sources.

To measure the stress strain data for the sand, a single grain was set on top of a steel plate. Force was then applied to the grain of sand by pressing down on a force gauge, which had a small piece of steel attached to the end. This piece of steel prevented the force gauge from being dented by the grain of sand. The Photron high speed camera took video of the event, and strain data was extracted from this footage. Figure 2.7 shows what a typical frame from one of these videos would look like.

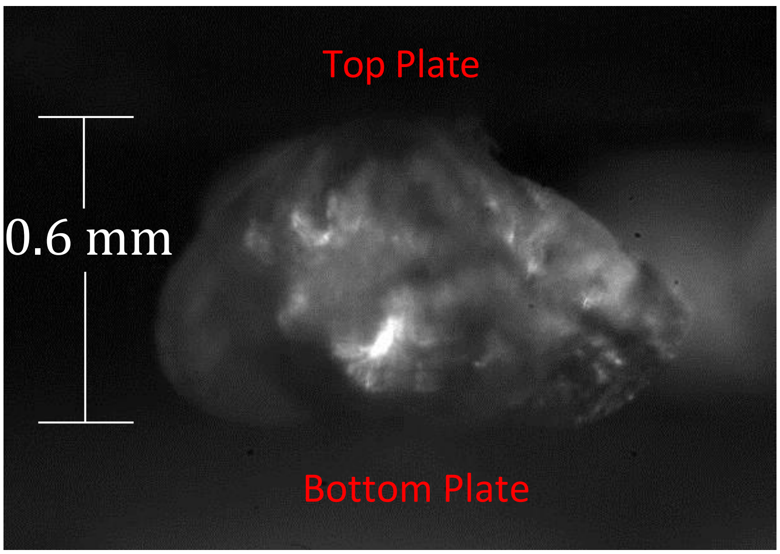

Figure 2.7. Sample image from the single grain experiments.

2.3. Ultrasonic Experimental Setup

The objective of the ultrasonic experiments was to determine if the compaction or damage waves observed during the penetration event were related to longitudinal or shear wave speeds of the sand. In order to do this, the longitudinal and shear wave speeds needed to be calculated. An Olympus Model 5058PR Ultrasonic Pulser/Receiver, along with an Agilent Technologies DSO6054A Oscilloscope was used to take these measurements. Figure 2.8 shows the equipment used in this experiment.

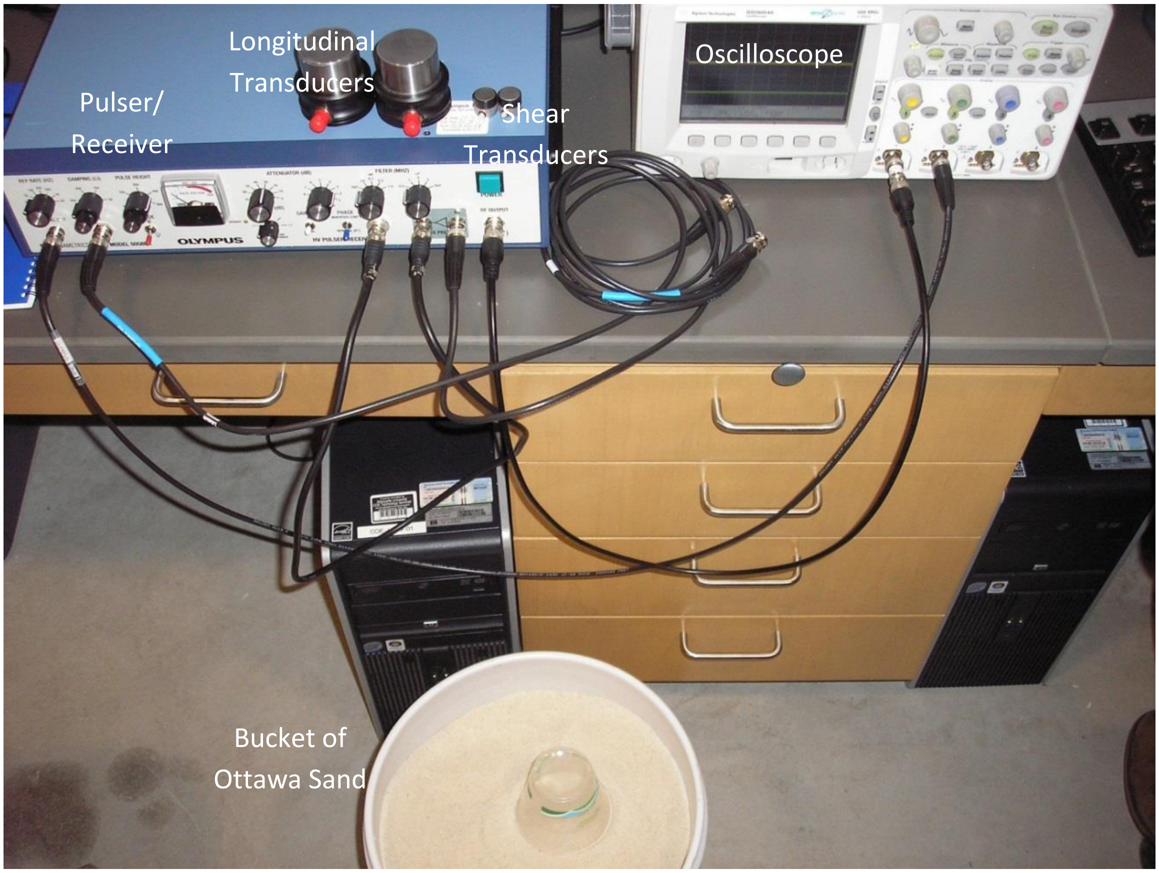

Figure 2.8. The Ultrasonic Pulser/Reciever, oscilloscope, transducers, and sand used in the ultrasonic experiments.

The pulser/receiver creates a pulse of energy, which the transducer will then make into a longitudinal or shear wave, depending on the type of transducer used. This wave will travel through the material, until it reaches the other transducer, which receives the wave. The resulting signal goes into the built in Auxiliary Preamp of the pulser/receiver, and then it is sent to the oscilloscope for data collection. The amount of time it takes for the signal to reach the receiver probe is recorded on the oscilloscope. An example oscilloscope trace is shown in Figure 2.9. The vertical yellow dotted lines show the timing of the initial pulse and the arrival of the pulse to the receiver probe. Knowing this timing and the distance between the probes, the speed of sound through the sand can be calculated. Figure 2.10 shows the configuration used in the first experiment.

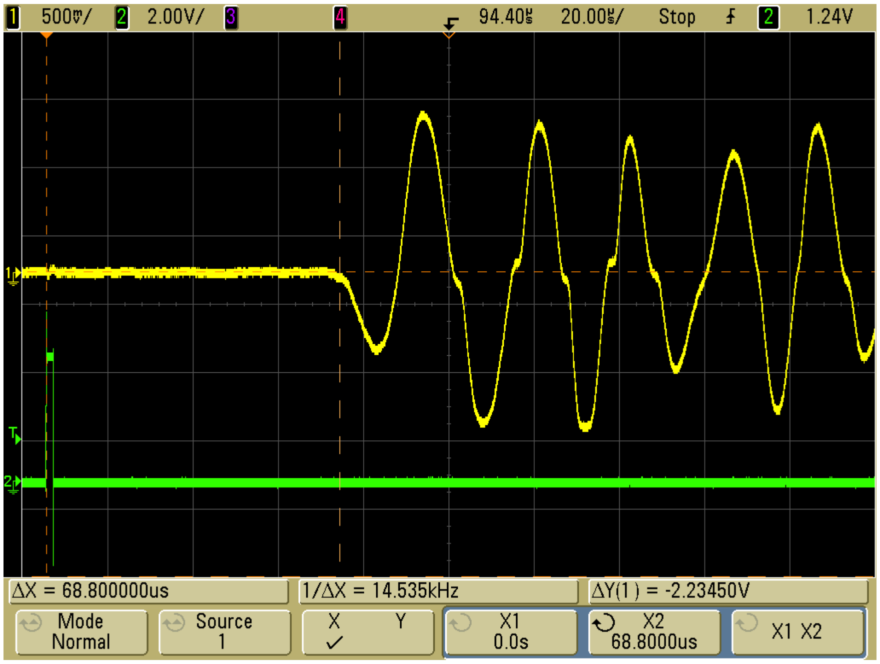

Figure 2.9. Example oscilloscope trace.

Figure 2.10. Configuration of the longitudinal transducers embedded in sand.

The objective of the second part of this experiment was to determine the effect of adding water to the sand to make it wet. To get this data, a slightly different experimental setup was used. The first difference was that the probes and sand were oriented vertically, as is shown in Figure 2.11, rather than horizontally as is shown in Figure 2.10.

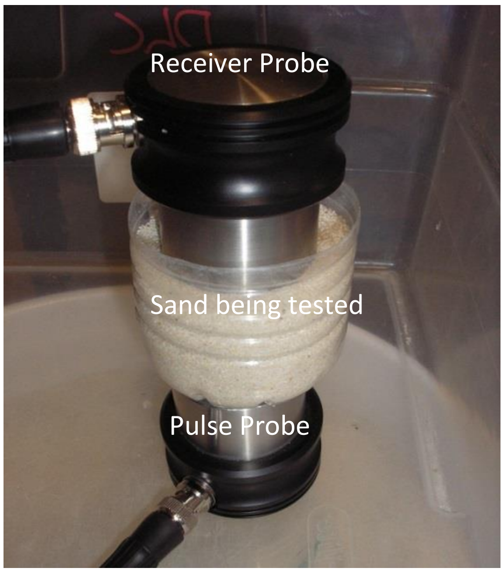

Figure 2.11. Experimental configuration for the wet sand tests, vertical orientation.

In order to take measurements of wet sand, it is desirable to know the mass of water in the sand. This means that the container holding the wet sand must be water proof, which is why a plastic water bottle bottom was used. The bottom of the water bottle could have introduced error if not taken into account, so the height of the bottom of the bottle as well as the time it took a longitudinal wave to pass through the bottom of the bottle were measured. The height was .375 in and the time it took was 13 μs. These were subtracted from all subsequent measurements to make sure no error was introduced.

The next difference between this part of the experiment and earlier parts was the addition of water. It is desirable to know the mass of the sand as well as the mass of the water added. With these masses and knowledge of the volume of the container, density of the sand

and of the solution can be calculated. The procedure to measure the wave speed of the wet sand is as follows:

1. Measure the mass of the dry sand.
2. Measure the wave speed through the dry sand.
3. Measure the mass of water in the pouring bottle.
4. Pour water into the dry sand.
5. Mix thoroughly.
6. Measure the mass of the wet sand, and that of the water in the pouring bottle.
7. Measure the wave speed of the wet sand.
8. Repeat steps 4 through 7 until the sand is saturated and that wave speed has been measured. The sand is considered saturated if after mixing there is a small amount of standing water on top of the sand.

2.4. EMU Peridynamic Formulation

The majority of continuum simulation codes utilize differential equations to solve for the variables used. The down side to these codes is that at a fracture surface there is a discontinuity, which causes these codes to breakdown. There are some workarounds to allow for fracture formation and propagation using these codes; however it cannot fully model the process of crack initiation and propagation. Peridynamic simulations use integral forms of the equations, which allows fracture to be more accurately modeled. EMU is peridynamic code that was created by Sandia National Laboratories, and it is currently in its alpha phase [17]. It does not utilize a mesh, rather each point has a certain area of influence. It is connected to and interacts with all other points within this sphere. If the points are stretched past a certain distance, the bond can irreversibly break, which is how cracks are created.

CHAPTER 3. EXPERIMENTAL RESULTS

3.1. Penetration Experimental Results

3.1.1. Initial Results

The first penetration tests were done with the target tank in a vertical orientation (the viewing window is parallel to the ground), rather than the configuration show in Figure 2.5. The result of one of these penetration events is shown in Figure 3.1. These images illustrate multiple important dynamic penetration mechanics, which is made possible by using a shutter speed that is too low. This allows a single image to show which grains of sand have moved during the time the shutter was open.

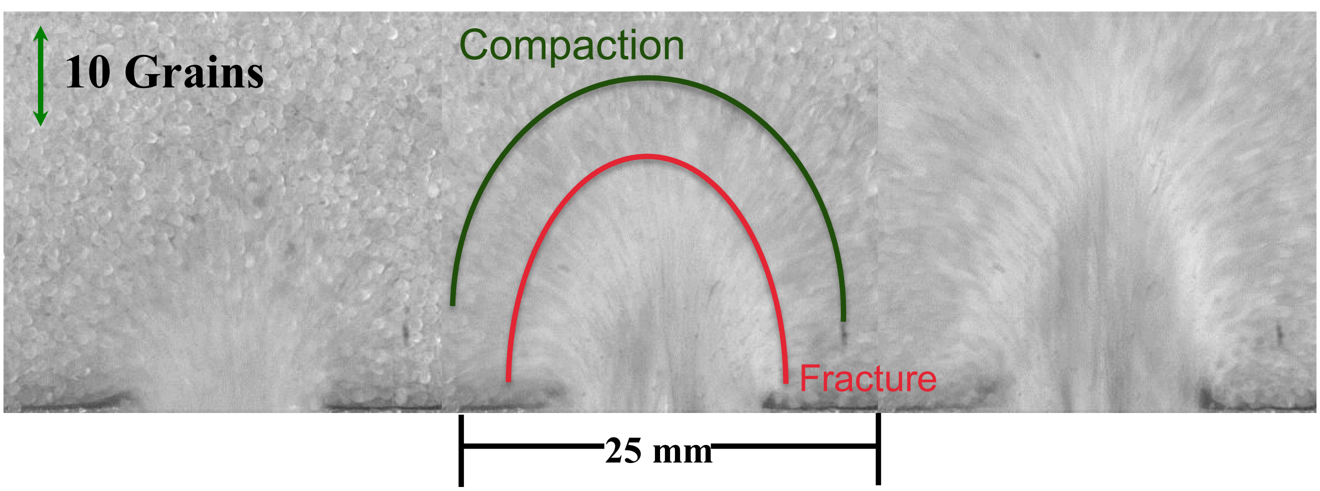

Figure 3.1. Three sequential frames of a penetration event, 55.6 µs apart.

In Figure 3.1 the creation of force chains is visible, which is demonstrated by the blur created by grains in the force chains moving before the dart directly acts upon them. The collective ends of all of the force chains make up the compaction wave. When a grain of sand is impacted by the compaction wave, it is the first time that the penetration event is affecting that grain. This compaction wave is what the pressure gauges measure. There is also an area of increased reflectivity directly in front of the dart. It was hypothesized that this increase in reflectivity is due to the creation of fracture faces as the grains are being damaged. This hypothesis was tested in the single grain experiments, the results of which are presented in Chapter 3.2.

Results similar to that of Figure 3.1 are typical for velocities between 35 and 100 m/s. Penetration events at velocities below 35 m/s did not show evidence of the fracture wave, the dart simply pushed the grains aside.

3.1.2. Investigating the Use of Hollow Darts

In order to obtain faster launch velocities, as well as having more control over the mass of the projectile, the use of hollow darts was investigated. The darts were created by using a solid dart for the tip, and using a hollow tube for the back of the dart. The tip and body of the dart were attached to each other by creating a stepped down diameter in the back of the tip, placing super glue around this diameter, and placing the hollow dart around it. The finished dart was of the same length and outer diameter as a solid dart, but considerably less weight.

It was discovered that using hollow darts decreased the integrity of the darts. The darts often did not follow a straight trajectory after entering the sand tank, including impacting the viewing window. There was also evidence that as the hollow dart was leaving the sabot, there was a vacuum effect pulling the dart back. The evidence for this is that the hollow end of the dart was extruded when we removed it from the target tank. Figure 3.2 shows all three of these

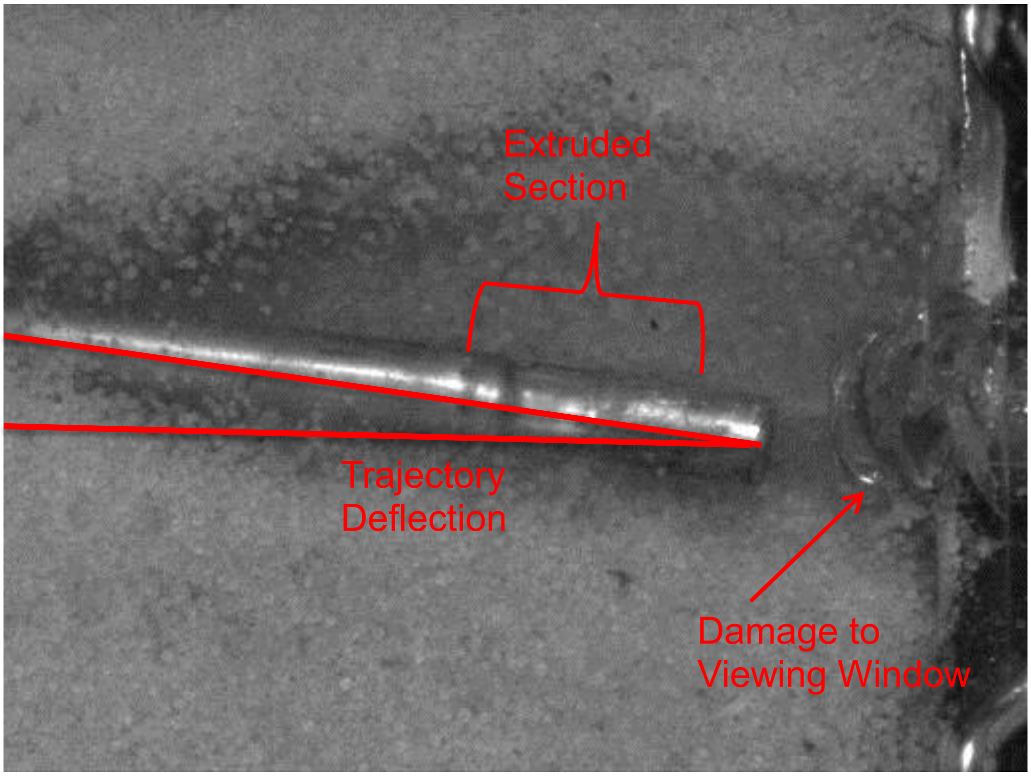

problems in a single shot.

Figure 3.2. Examples of problems created by using hollow darts.

An attempt was made to prevent the vacuum effect by adding notches into the hollow section of the dart, which would allow air to flow in. This further decreased the strength of the hollow section of the dart. This made the other problems more pronounced, and did not do a good job of reducing the extrusion that the dart underwent.

3.1.3. Effects of Dart Nose Shape and Pressure

The effect that the shape of the nose of the dart and the pressure in the sand had on the penetration event was investigated next. As is shown in Figure 2, three different dart types were used. There were three different pressure conditions used, listed in increasing pressure order: free surface (there is air directly above the sand), fixed surface (pressure plate above sand, but no pressure added), and moderate pressure. The moderate pressure condition is subjective; however the same person added the pressure each time so the variability was minimized.

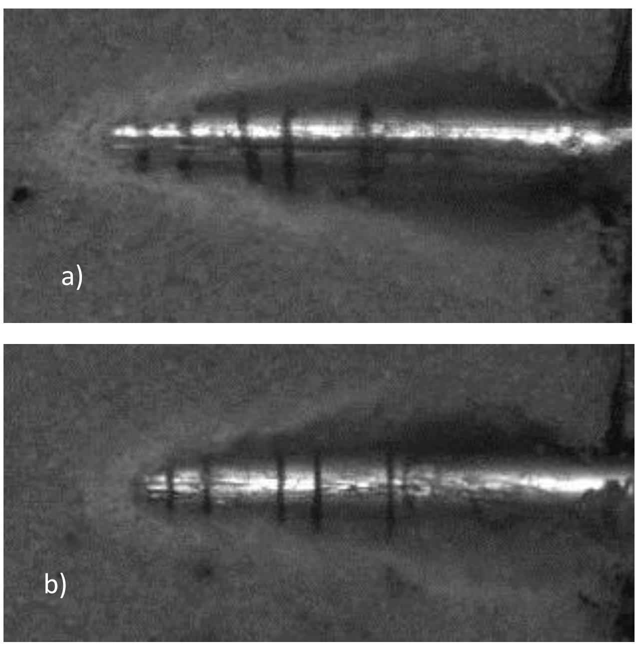

Figure 3.3. The fracture cone around a) flat nose and b) hemispherical nose darts with a free boundary condition.

Figure 3.3 shows how the dart nose shape affects the visible fracture cone. The flat nose dart has a fracture cone that extends further forward in the direction that the dart is traveling, as well as having a longer trail. This is believed to be due to the increased ability of the hemispherical dart to push through the grains of sand, meaning these darts require fewer grains to be fractured. The size and shape of the cavity formed by the dart penetration is approximately the same.

The pressure on the sand also has an effect on both the fracture cone and cavity that is created. As the pressure in the sand increases, the resistance to the dart pushing through the grains also increases, which causes the darts to fracture more grains during the penetration event. This effect is shown in Figure 3.4, where the fracture cone increases in size as the pressure in the sand increases. It is also evident that the size of the cavity decreases as the pressure in the sand increases.

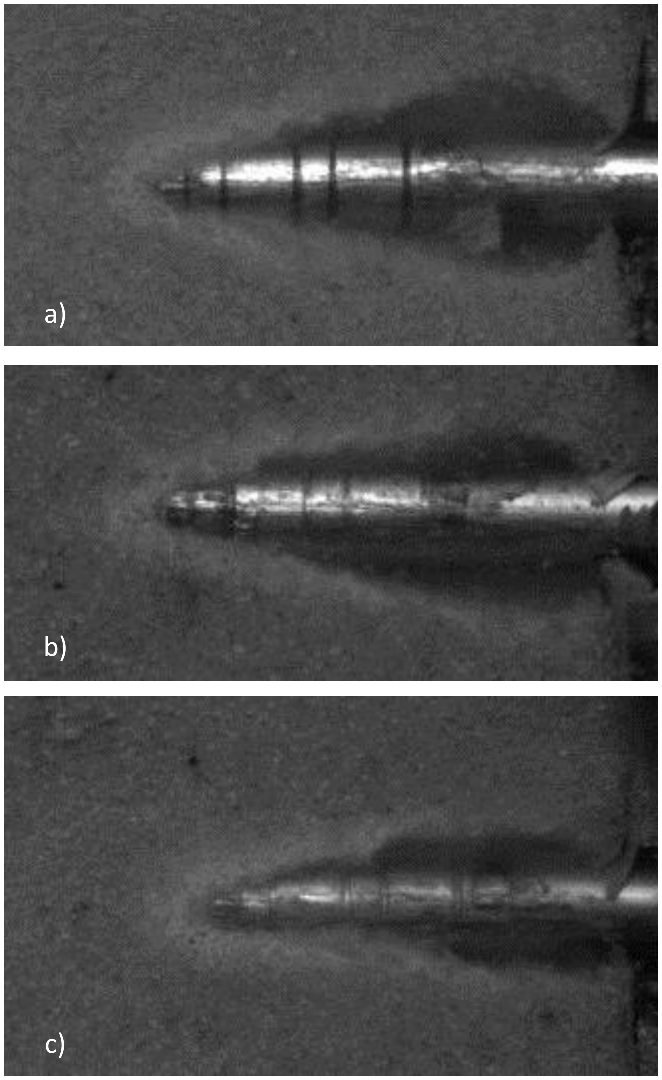

Figure 3.4. Penetration characteristics of flat nose darts with a) free surface, b) fixed surface, and c) moderate pressure.

Similar to Figure 3.3, Figure 3.5 shows the difference between a flat nose and a conical nose dart, this time with moderate pressure on the sand. The moderate pressure on the sand makes the difference between the dart nose shapes even more evident, the fracture cone on the flat nose dart is much brighter and bigger. With the increased penetration resistance of the sand at a medium pressure, the ability of the conical nose dart to push its way between the grains of sand creates much less fracture in the sand.

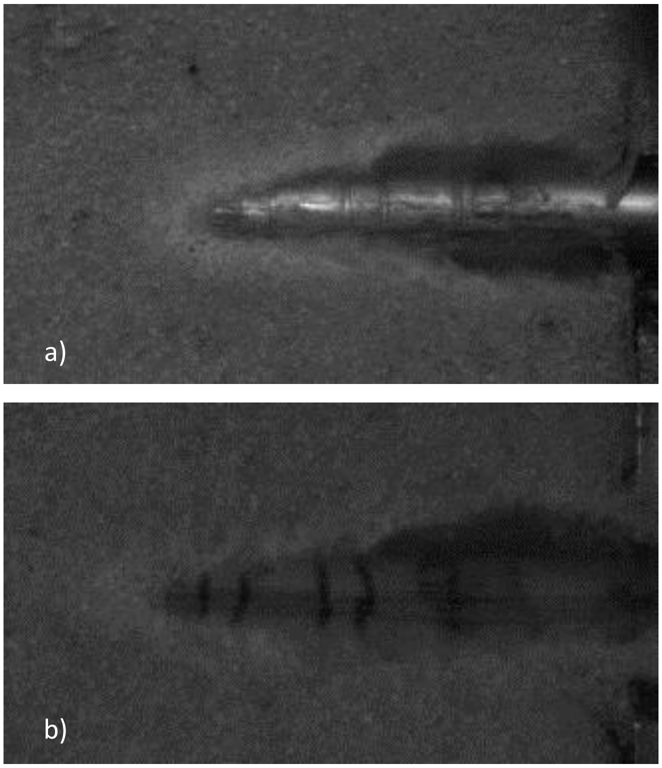

Figure 3.5. Penetration characteristics for darts in moderate pressure with a) flat nose and b) conical nose.

The way the penetration event is affected by the pressure of the sand can also be seen by looking at the data gathered from the quartz pressure gauges. Figure 3.6 shows the pressure profile given from a quartz pressure gauge with the three different pressure configurations. This data is from the first pressure gauge, which was placed 25mm above the shot line and 25mm behind the target tank entrance for all penetration events. There are three important observations that can be made about the data in Figure 3.6. First, the speed of the compaction wave increases as the pressure in the sand increases, which is shown by compaction wave reaching the pressure gauge earlier in the increased pressure situations. Second, there is an increase in the reverberation waves in the sand in the increased pressure, especially in the transition from free surface to fixed surface. Third, there is a decrease in the noise that the pressure sensor measures as the pressure increases, which can be attributed to a more compact granular material with more persistent force chains.

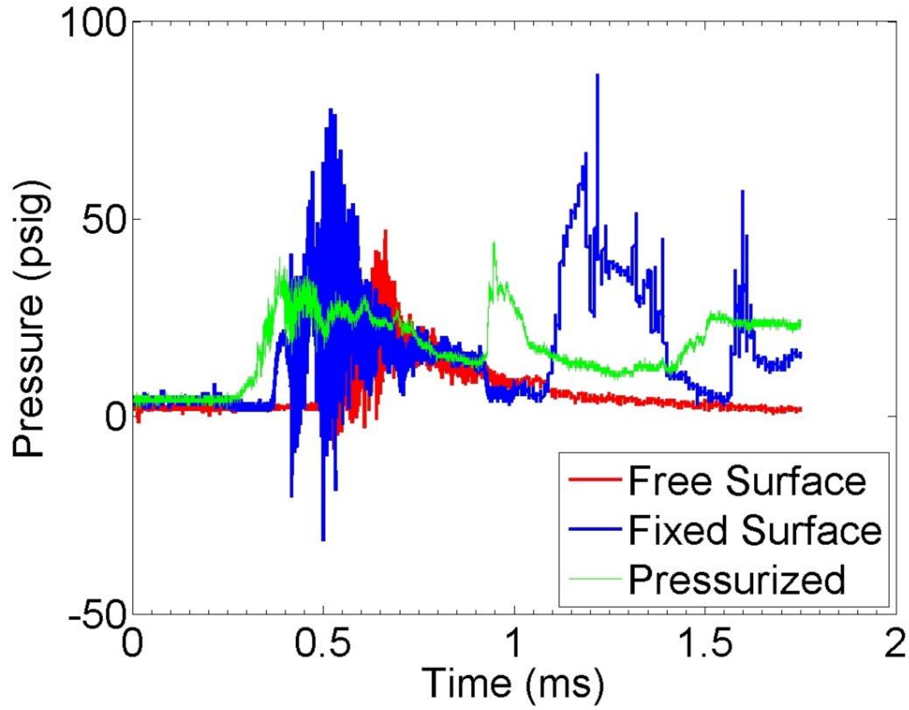

Figure 3.6. Pressure traces for the three different pressure configurations.

The depth that a dart can penetrate into the sand tank can also show how nose shape and pressure can affect the penetration event. The experiment was not designed as a semi-infinite target tank, which would be ideal to measure the depth of penetration; however, some useful insight can be gleaned. When the pressure plate is free or fixed, the darts travel through the field of view and impact the back of the target tank. When a moderate pressure is applied to the sand, the darts come to rest before leaving the field of view. This shows that the resistance to penetration is increased as the pressure in the tank of sand is increased, which was hypothesized from the size of the fracture cone at different pressures. Table 3.1 shows the depths of penetration that the darts reach. We see that at the moderate pressure level, conical nose darts penetrate the furthest and flat nose darts penetrate the least. This validates the previous hypothesis that conical and hemispherical nose darts penetrate through the sand more easily than flat nose darts do.

Table 3.1. Depth of penetration for different nose shape and pressure configurations.

	Free Surface	Fixed Surface	Pressurized
Flat Nose	9+ in	9+ in	5.6 in
Hemi Nose	9+ in	9+ in	6 in
Cone Nose	N/A	9+ in	6.6 in

3.1.4. Particle Image Velocimetry Results

Using MPIV, Matlab particle image velocimetry toolbox, it is possible to get data for the velocity field for regions of sand in the target tank [16]. From the images that MPIV creates we can see the relative velocities of different regions of the sand. Figure 3.7 is an example MPIV image result.

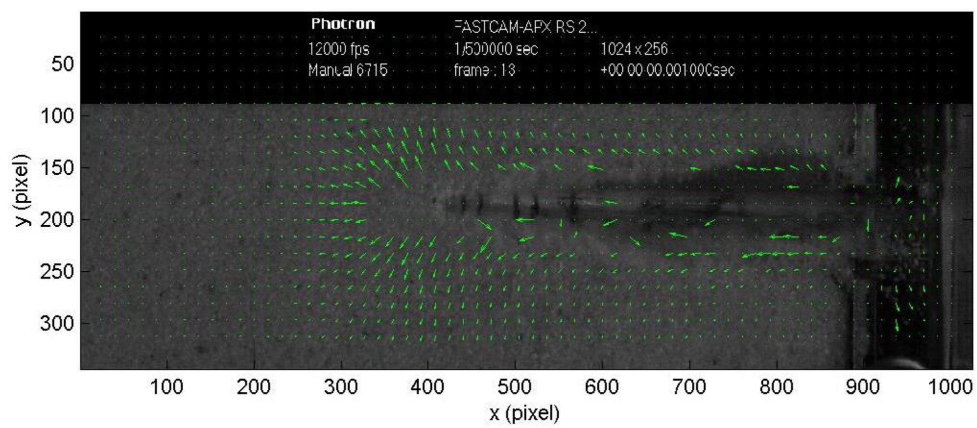

Figure 3.7. Example MPIV image.

From the images that MPIV creates, we can understand which areas of the target box are being influenced by the penetration event. Areas that have no velocity have not yet been hit by the compaction wave. The MPIV software cannot resolve the velocity for regions where there is grain damage, where there are no particles (along the dart and in the cavity), or where the velocity of the sand is too great. It does show that the majority of momentum imparted on the sand near to the shot is in a direction parallel to the shot line. It also shows that the majority of the momentum imparted onto sand away from the shot line (near the top and bottom of the tank) is in a direction perpendicular to the shot line.

3.1.5. Naval Surface Warfare Center – Indian Head Results

Experiments were run at the Naval Surface Warfare Center at Indian Head (NSWC-IH) which allowed us to use the Cordin 550 camera that NSWC-IH has. The other main difference between the setup at NSWC-IH and the setup at Marquette, is that at NSWC-IH Helium was used as the working gas instead of air. The penetration velocities attained were still near 100 m/s, so this change did not have an impact on the penetration event.

One observation made from these experiments is that during the penetration event, not all grains in the fracture cone are completely destroyed. Some of these grains are pushed along directly ahead of the dart for distances on the order of at least 10x the length of the grain of sand. These grains may be stronger in the orientation they happen to be in, or they may be fitting in between the force chains, and therefore not having a large amount of force being applied to them. Evidence for these grains that are simply pushed along in front of the dart is in Figure 3.8, which shows the same grain of sand directly in front of the dart in images 35 frames apart (87 µs).

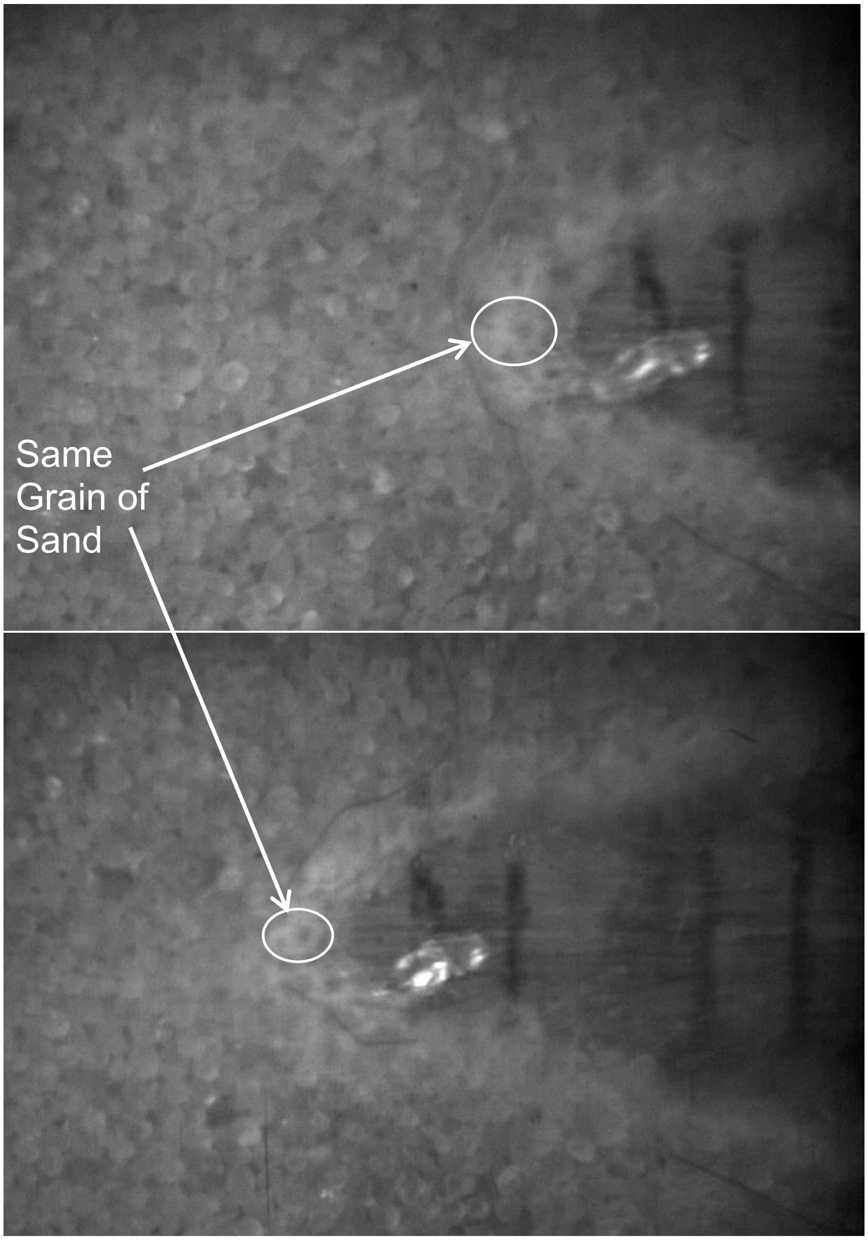

Figure 3.8. Images showing the same grain of sand, 35 frames and 87 µs apart.

The Cordin 550 camera along with a smaller field of view allowed for the visual confirmation of phenomenon that were previously assumed, specifically the formation of force chains in a dynamic penetration event. Figure 3.9 shows the progression of a grain of during a penetration event. First the grain is not being affected by the penetration event, second it becomes part of a force chain, and third it is fractured.

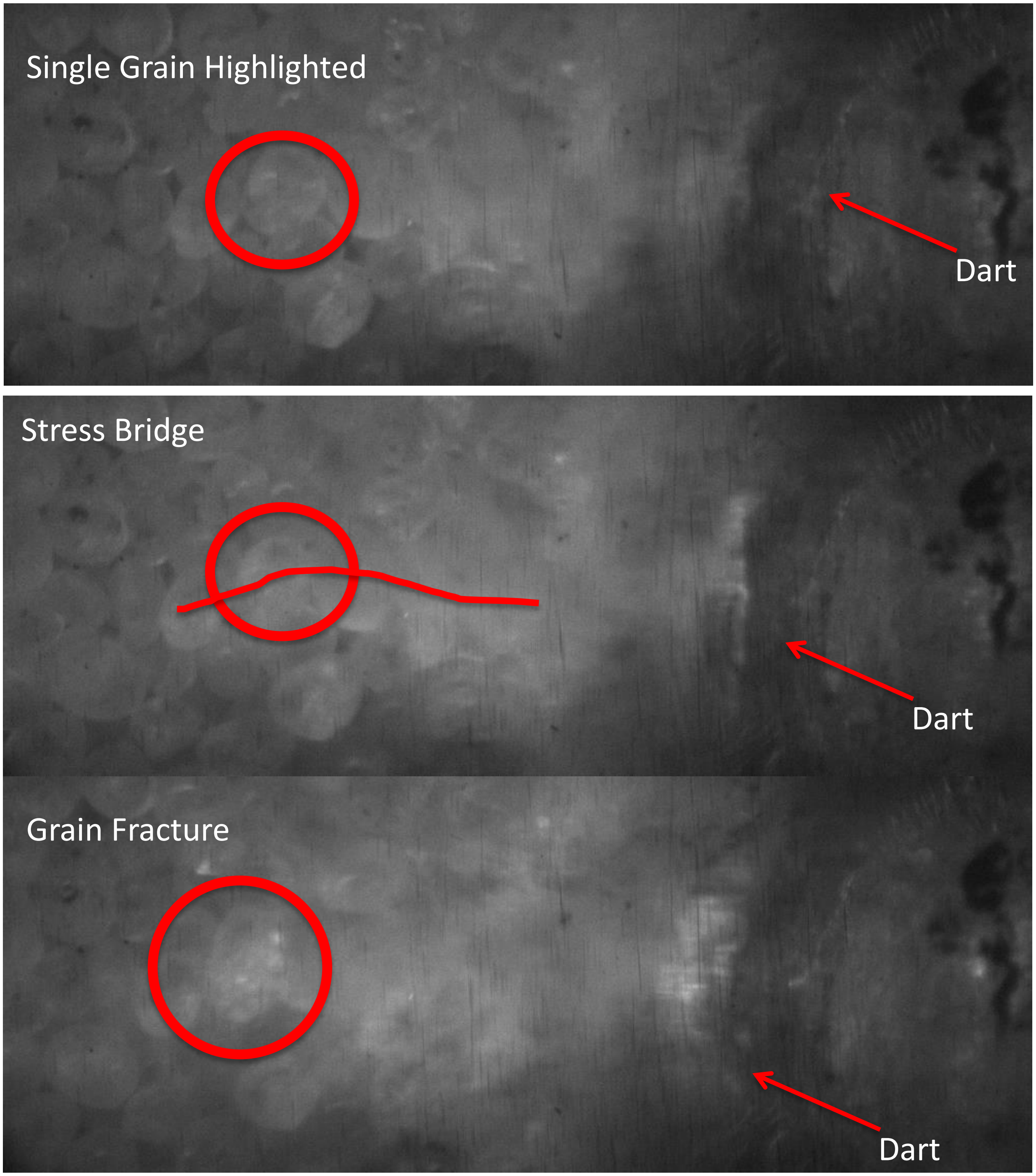

Figure 3.9. Shows the progression of a grain during a penetration event.

3.2. Single Grain Experimental Results

3.2.1. Fracture Reflectance Confirmation

In this set of experiments, the objectives were: to determine if the increased brightness observed in the fracture cone was due to reflectance off of a fracture surface and to determine if there was triboluminescence. It was found that the increased reflectivity was indeed caused by the fracture of the grains of sand. Figure 3.10 shows a single grain of sand before and after a crack has formed.

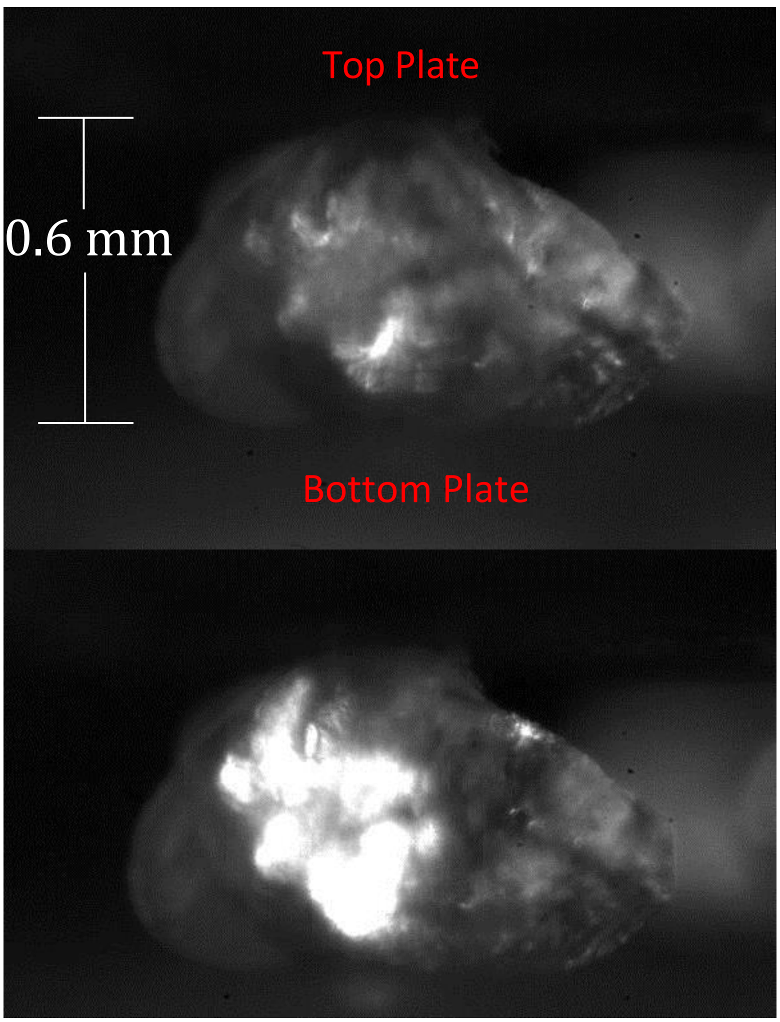

Figure 3.10. Images of a single grain of sand before and after a crack has formed.

This experiment was repeated 10 times, with each test, the sand grain showed an increase in reflection from fracture. This was then repeated five more times, but without the

Halogen light shining on the grain of sand. In these tests the camera did not pick up any light, which means that we can conclusively say that triboluminescence is not the reason for this phenomenon present in the fracture cone. We cannot conclusively say that the grain does not triboluminesce, but it is not the main cause of the visible fracture cone.

3.2.2. Single Grain Stress-Strain Results

Single grains of sand were crushed in the method described in Section 2.2 to gather stress strain data. In order to understand the stress-strain data it is important to understand the morphology of how the grains fracture in this experiment. The grains are initially unloaded, and are then loaded until they undergo catastrophic failure. Before these grains catastrophically fail, there are generally multiple smaller fractures. These small fractures can be crack formation, flake fractures (where flakes fly off of the grain of sand), or grains being fractured into multiple pieces. Figure 3.11 shows a grain as starts as completely intact, then a fracture face forms, the flakes fracture off, and finally it undergoes catastrophic failure.

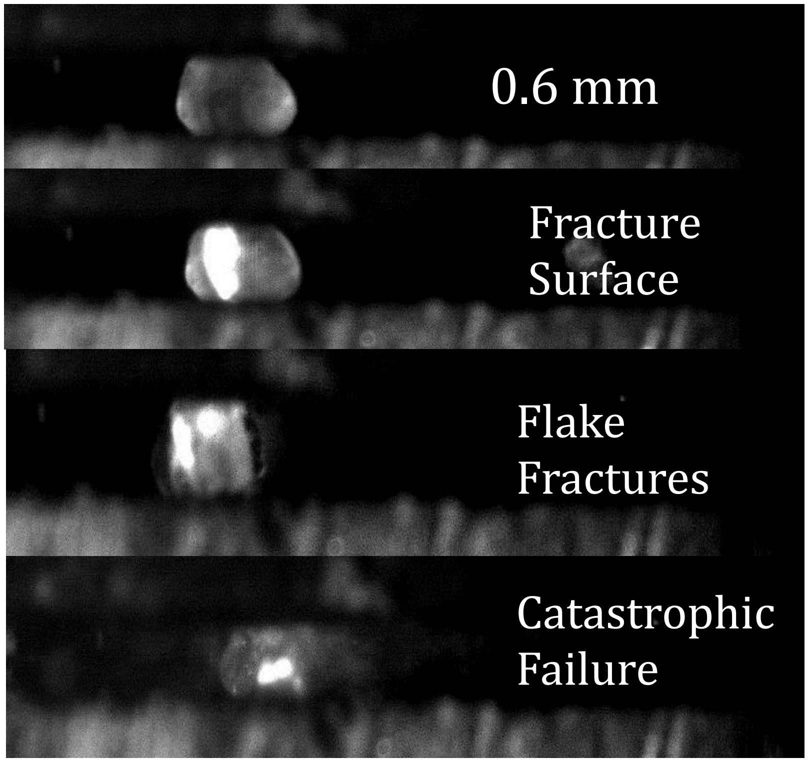

Figure 3.11. The morphology of the fracture of a single grain of sand.

The stress strain data for the sand is shown in Figure 3.12. The strain data for the points labeled as 2nd fracture is not a true strain value, because it often happened that the height of the grain of sand decreased greatly when large pieces of the grain of sand fractured off. This data is meant to give an approximate envelope of the stress-strain relationship for use in peridynamic simulations. Hopkinson Bar data for the stress strain relationship of α-quartz is plotted with the data, to show that the data is reasonable.

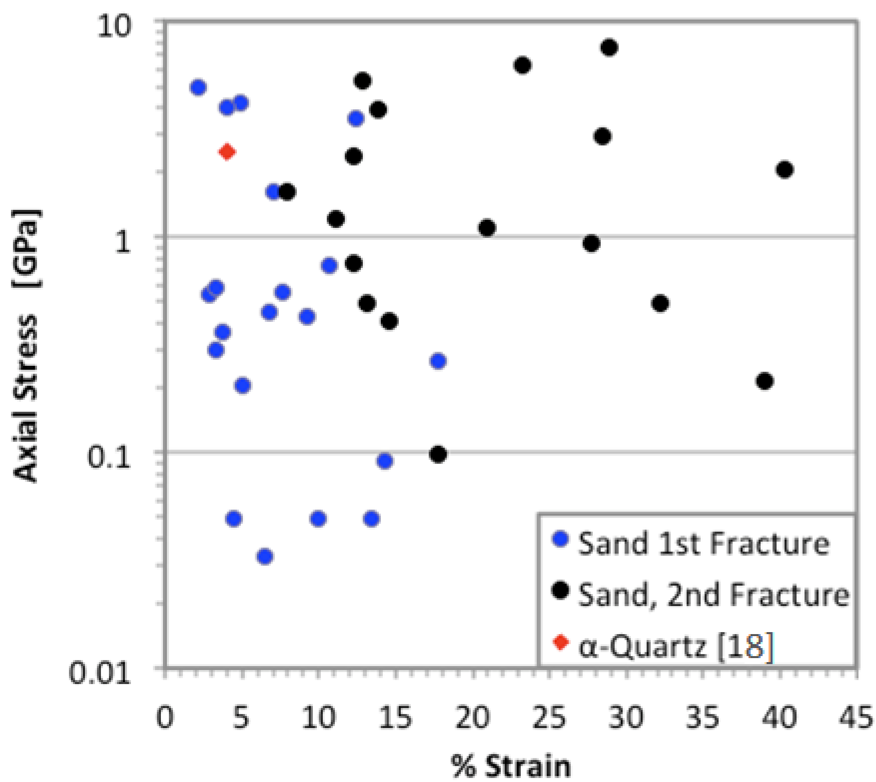

Figure 3.12. Stress-strain data for single grains of sand, with Hopkinson Bar data for pure α-quartz included [18].

This data shows that grains of sand sometimes have weak sections and/or orientations. Once these sections have been fractured off, it is possible that the strength of the grain will increase. This could explain the observation made in Section 3.1.5 that some grains are partially fractured but afterwards the remainder stays intact and is pushed in front of the dart.

3.3. Ultrasonic Experimental Results

3.3.1. Longitudinal and Shear Wave Speed Verification

In order to confirm that the equipment used in these experiments would accurately measure the speed of sound in a material some verification tests were done. The verification materials used were Poly(methyl methacrylate) (PMMA aka Plexiglas), aluminum

6061, and air. The results for these verification tests can be found in Table 1. The literature longitudinal wave speed for aluminum was calculated using the following equation and data for the density and elastic modulus of 6061 aluminum[19].

$$E = \rho * {c_l}^2 \tag{1}$$

where E is the modulus of elasticity in Pa, ρ is the density in kg/m^3, and c_l is the longitudinal wave speed in m/s. Equation 1 can be rearranged to solve for c_l, yielding the following equation.

$$c_l = \sqrt{\frac{E}{\rho}} \tag{2}$$

Table 3.2. Results of verification tests for longitudinal wave speeds [20].

Material	Measured c_l (m/s)	Literature c_l (m/s)	Percent Error (%)
PMMA (Plexiglas)	2303	2690	14.37
6061 Aluminum	4669	5052	7.58
Air	348	343	1.43

Table 3.2 shows that this method for determining wave speed is an accurate measurement technique. The higher error for PMMA is likely caused by comparing similar but not identical materials. PMMA can have a range of mechanical properties based on the method of manufacturing and the exact chemical characteristics of the material. These possible differences in the material could account for this larger error in relation to the percent error found through air. Likewise aluminum also has uncertain material properties. The longitudinal wave speed, c_l, is calculated using the density and elastic modulus for the material, which is given as a range of values even for a specific grade of aluminum in literature. This leads us to

believe that the actual error using this measurement technique is in the 1-5% range, which is based on the percent error of the wave speed through air.

After the longitudinal wave speeds were verified, the shear wave speeds were also verified. This experiment compared the shear wave speed through PMMA and 6061 aluminum to literature values. Air was not used in this experiment because shear waves (aka transverse waves) only travel through solids (i.e. materials with non-zero shear modulus). The results for these verification tests can be found in Table 3.3. The literature shear wave speed for aluminum was calculated using the following equation and data for the density and shear modulus of 6061 aluminum [19].

$$G = \rho * {c_s}^2 \tag{3}$$

where G is the shear modulus in Pa, ρ is the density in kg/m^3, and c_s is the shear wave speed in m/s. Equation 3 can be rearranged to solve for c_l, yielding the following equation.

$$c_s = \sqrt{\frac{G}{\rho}} \tag{4}$$

Table 3.3. Results of verification tests for shear wave speeds [20].

Material	Measured c_s (m/s)	Literature c_s (m/s)	Percent Error (%)
PMMA (Plexiglas)	1258	1340	6.14
6061 Aluminum	3092	3103	0.348

Table 3 shows that this method for determining wave speed is an accurate measurement technique. The error for these calculations appears to be even less than those of the longitudinal wave speeds. This appears to be true even though smaller wave travel distances had to be used because the excitation pulse voltage used with the shear transducer cannot exceed 100 V, whereas the longitudinal transducer could utilize excitation pulses up to 900 V. Using a short travel distance means that small inaccuracies in measuring the travel distance or travel time will have a large effect on the measured wave speed.

3.3.2. Longitudinal and Shear Wave Speed through Dry Sand

The objective of this experiment was to find the longitudinal wave speed through Ottawa sand. In these experiments the sand was dry and in an "*as poured*" configuration, thus no packing or shackling. The wave speed was measured three times, using various distances through the sand. The configuration used is shown in Figure 2.10. The results were averaged to give the longitudinal wave speed. These results are shown in Table 3.4.

Table 3.4. Longitudinal sound speed values through dry "as poured" Ottawa sand.

Trial	1	2	3	Average
c_l (m/s)	270	254	263	263

The differences in longitudinal wave speed values for different trials can be attributed to the random nature of dealing with *as poured* granular materials, as well as measurement error. Slight differences in density as a result of random packing may have an effect on the wave speed. The longitudinal sound speed through solid quartz was calculated, using Equation 2, to be 5383 m/s. It is clear that the longitudinal sound speed through sand is not the same as through solid quartz. The sound speed is a function of dynamics of the granular medium, and not just based on the solid material characteristics.

The second part of this experiment was to find the shear wave speed through as poured Ottawa sand. The wave speed was measured twice, using various distances through the sand, and those results were averaged to give the shear wave speed. These results are shown in Table 3.5.

Table 3.5. Shear sound speed values through dry "as poured" Ottawa sand.

Trial	1	2	Average
c_s (m/s)	230	186	209

Part of the difference in shear wave speed values for different trials can be attributed to the random nature of dealing with as poured granular materials. Slight differences in density as a result of random packing will have an effect on the wave speed. This variance may also be due to error associated with using a short travel distance (less than 5cm).

The shear sound speed through solid quartz was calculated, using Equation 4, to be 3435 m/s. It is clear that the shear sound speed through sand is not the same as through solid quartz. The shear sound speed is a function of dynamics of the granular medium, and not just based on the solid material characteristics, just as it is for the longitudinal sound speed.

3.3.4. Comparison of Shear, Longitudinal, Compaction, and Fracture Waves

This experiment compared the wave speeds calculated in parts Section 3.3.2 to the compaction and damage wave speeds observed in a dart penetration event. Figure 3.13 shows the average velocity of the dart and the various waves as a function of video frame.

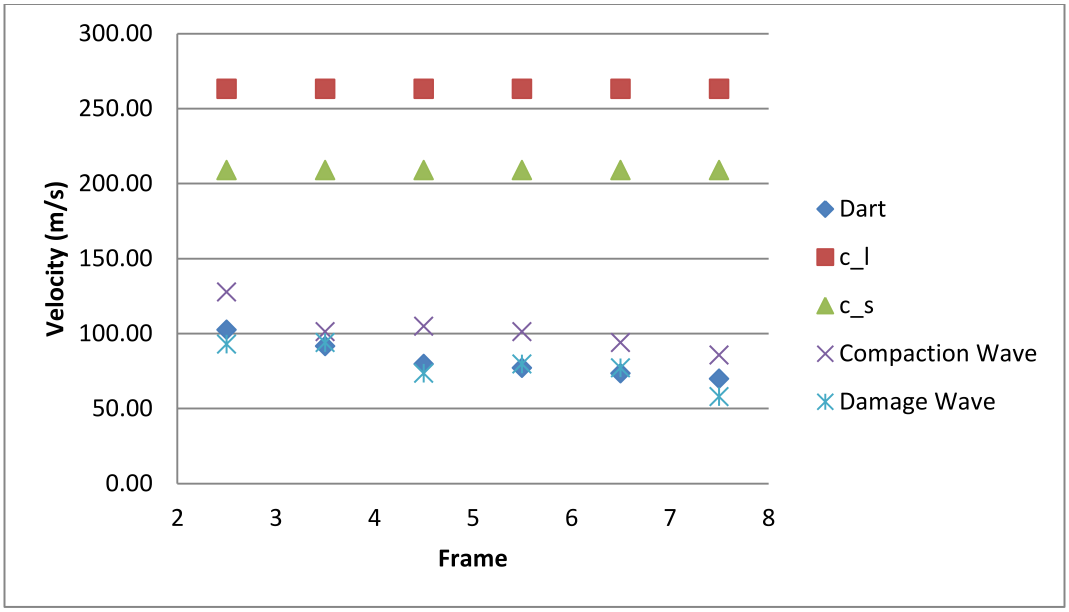

Figure 3.13. Plot of the average dart velocity vs frame for various wave types, with an inter-frame time of 83 μs.

The damage waves observed in videos of the sand penetration event, see Figure 3.13, correspond closely to the speed of the dart in the sand, and do not seem to be related to the longitudinal or shear wave speeds. In addition, it appears that the damage wave speed is approximately equal to the speed of the dart. This is shown in Figure 3.14, which shows the length of the damage wave as well as the distance between the compaction wave and the dart as a function of frame.

In Section 3.1.3 it was found that increased hydro-static pressure in the sand would increase the speed of the compaction wave. It is also evident from Equations 2 and 4, that as the pressure and therefore the density increases, the longitudinal and shear wave speeds are also increased. This is a shared feature of these wave speeds, and not evidence that they are proportional to each other.

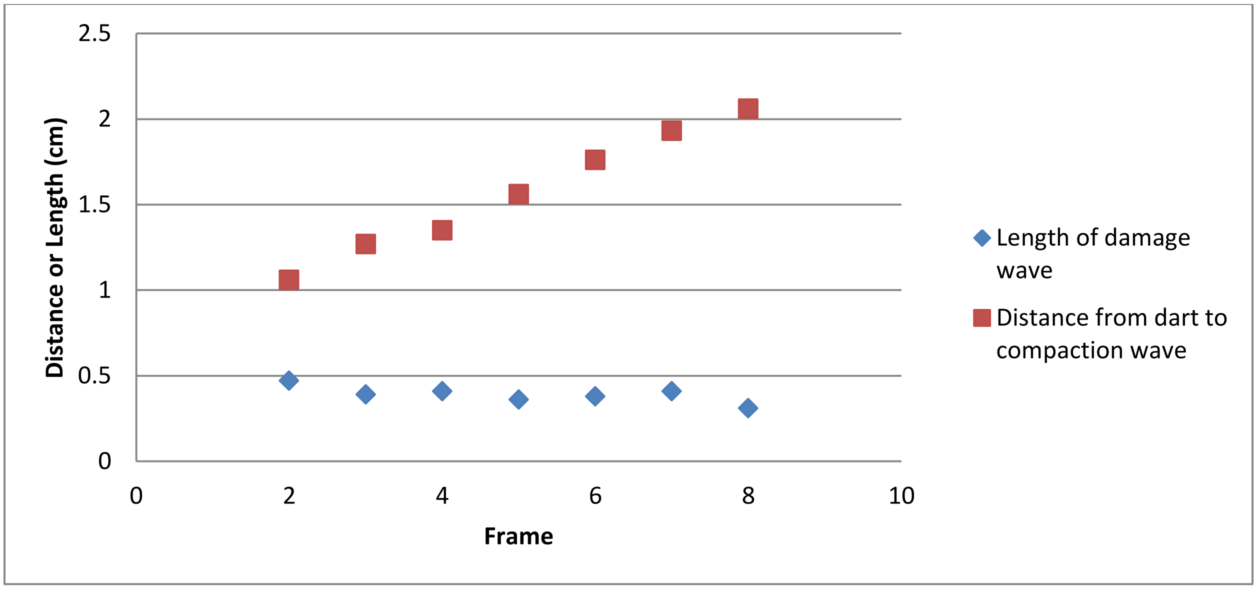

Figure 3.14. Plot of various distances vs. frame with an inter-frame time of 83 µs..

Figure 3.14 shows that the length of the damage wave is constant through this section of the penetration event. It also shows that the distance from the dart to the compaction wave increases linearly, which indicates a constant difference in velocity between the dart and the compaction wave.

3.3.5 Longitudinal Wave Speed in Wet Sand

The wave speed of wet sand was calculated using the procedure denoted in Section 2.2. The significant results from completing this procedure are listed in Table 3.6, note that the wave speed through pure water was also measured.

Table 3.6. Wave Speed of Wet Sand Results

Material	Wave Speed (m/s)	Sand Density (kg/m^3)	Solution Density (kg/m^3)	Percent water by mass (%)
Dry Sand	274	2006	2006	0
Wet Sand 1	218	1850	1923	3.81
Wet Sand 2	216	1803	2067	12.78
Wet Sand 3 (Saturated)	255	2022	2470	18.15
Water	1456			

From Table 3.6 we can see that once water is added the wave speed decreases greatly, and it slowly returns to higher values as the water content approaches saturation. We see a similar trend for the density of the sand. It is known, and can be seen in Equation 1, that the wave speed is dependent on density. This trend is shown in Figure 3.15, which plots the longitudinal wave speed vs density.

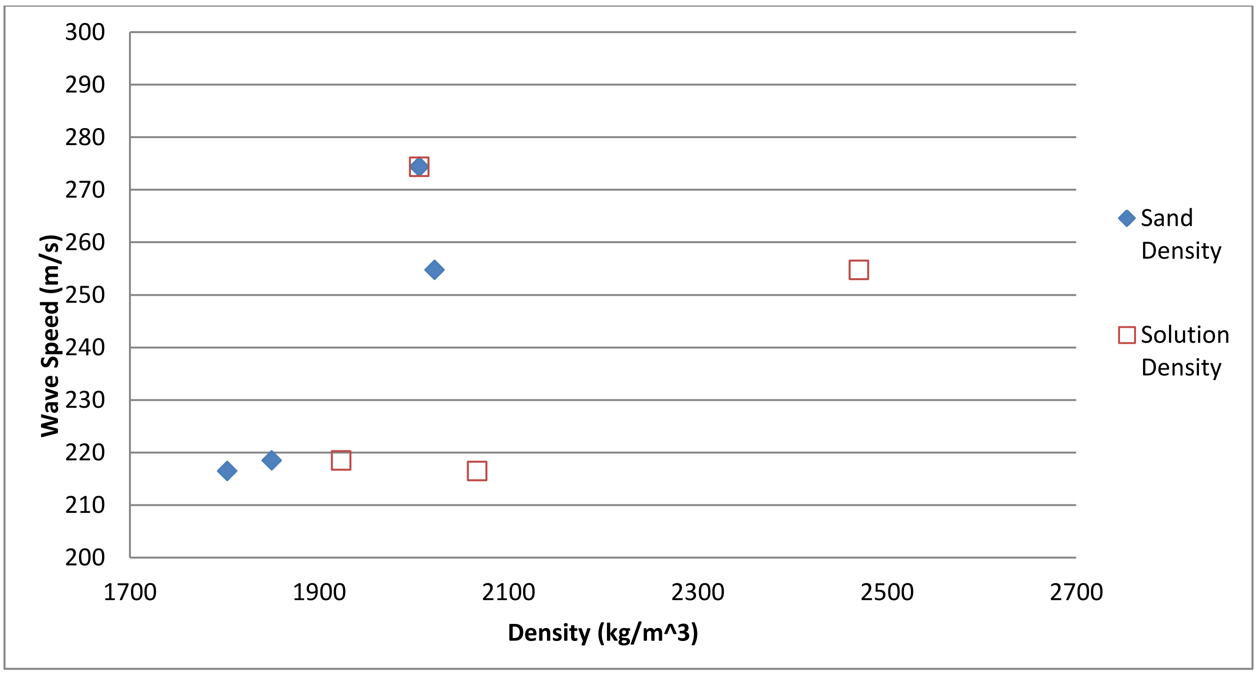

Figure 3.15. Plot of wave speed vs sand density and solution density.

The blue diamonds use the density of the sand, while the red squares use the density of the solution (sand + water). It appears that there is a linear relationship between sound speed and sand density. We would expect from Equation 2 that it would scale with $\sqrt{\frac{1}{\rho}}$. It does not appear that there is an obvious relationship between the solution density and the wave speed. This indicates that the wave speed measured, even when the sand has become saturated, is related to the sound speed of sand and not water. This is further confirmed that considering that the sound speed in water is about 1450 m/s, which is much greater than the sound speeds calculated for wet sand.

3.4. Numerical Simulation Results

A simulation in EMU was run using a dart impact speed of 100 m/s. There were much fewer grains of sand in the computational domain than in the target sand box, which was necessary to allow the simulation to run in a timely manner. The result of this simulation is show in Figure 3.16, in which damage is plotted. Damage is calculated as the percent of bonds that are broken for each cell, with red being completely damaged and blue being undamaged.

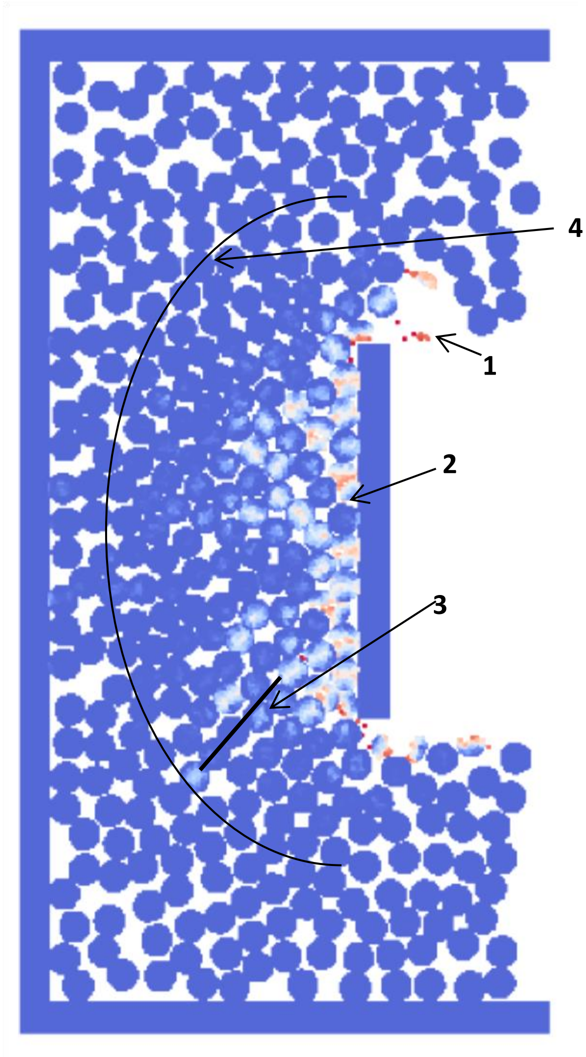

Figure 3.16. EMU simulation showing damage done to the sand.

This simulation does not fully model what is seen in the experiments, which is partially due to the scaled down nature of the simulation. There are many similarities between the result in figure 3.16 and what is observed in experiments. There are grains of sand which have been greatly damage, resulting in very small particles in the wake of the dart (1). There are also grains of sand in front of the dart which are not at all damaged even though grains in front of those grains are (2), as was observed in the NSWC-IH penetration experiments. There are also grains that are far out from the dart which are damaged (3), which is the result of force chains extending out in front of the dart. There is also a compaction wave traveling through the granular material (4), which is evidenced by increased density of the sand in a hemisphere around the dart.

CHAPTER 4. CONCLUSIONS AND FUTURE WORK

4.1 Penetration Experiments

In the initial results, a two wave structure was found to be the main mechanism for penetration. The compaction wave travels in front of the dart, and increases the density of the sand. There was also evidence of the existence of a fracture wave, where the damage done to grains of sand was visible due to increased reflectivity. This two wave structure was shown to exist for penetration velocities around 100 m/s. For penetration velocities around 35 m/s no fracture cone was evident.

Hollow darts were manufactured in an attempt to reach higher penetration velocities. It was found that the strength of these darts was not sufficient to allow for a repeatable penetration event. It may be possible to create a hollow dart using a different manufacturing method which would have more strength.

The effect of increasing the pressure in the sand is to cause the darts to fracture more grains of sand, rather than just pushing grains of sand out of the way. This is due to the pressure increase increasing the resistance of the sand to penetration, and this manifests visually as the fracture cone becoming more pronounced.

When darts with conical or hemispherical nose shapes are used, the ability for the dart to penetrate is increased. This is evident from these darts creating a smaller fracture cone, as well as these darts being able to penetrate deeper into the sand when there is a moderate amount of sand pressure being used.

MPIV was used to gather data on the flow field of the sand during a penetration event. This program was not able to resolve the velocity of sand in close proximity to the dart, nor sand that is traveling too fast. It did give a good visual for how different regions of the target tank are affected by the penetration event, which is useful in comparing to the velocity of grains in a numerical simulation.

Experiments were done at NSWC-IH with a Cordin 550 camera. The high resolution coupled with a small field of view allowed for the observation of a few new dynamic responses to the penetration event. Evidence was found for the creation of force chains. This is a well-known mechanic for the reaction of granular medium to static forces, but it was observed here for dynamic experiments. There was also evidence that some grains of sand could “ride along” with the dart without being destroyed.

There are some logical future experiments that could be done to increase the understanding of the penetration event. The air gun has been modified, and initial tests show that it can now accelerate darts to a penetration velocity of 150 m/s. It is of interest to study how this increase in penetration velocity interacts with the effects of pressure and nose shape. Experiments using the Cordin 550 camera at these penetration velocities could show evidence of important dynamic mechanisms at this higher velocity.

A static pressure gauge has been acquired. This will allow the static pressure in the sand to be measured. This will allow for putting actual numbers to the amount of pressure in the sand. It will also allow for a study into penetration depth as a function of pressure.

Once a more developed numerical simulation is developed, the vector field created from MPIV could be compared to the velocity of the grains of sand in EMU. It would also be of interest to create experiments that use wet sand instead of dry sand, since data for the wave speed through wet sand has already been calculated.

4.2 Single Grain Experiments

Experiments were done involving the crushing of a single grain of sand, which was filmed in both high and low light configurations. This experiment showed that there was an increased reflectivity as fracture faces were formed. It also showed that triboluminescence was not the main reason for the increased light in the fracture cone. Stress-strain data for the type of sand being used was also taken, to be used in the peridynamic simulations.

4.3 Ultrasonic Experiments

After a few verification tests, the longitudinal and shear wave speeds were calculated for as poured sand. These wave speeds were compared to the compaction and damage wave speeds observed in penetration experiments. It was found that the compaction and damage wave speeds did not correspond to the longitudinal or shear wave speeds. In the future, an experiment could be set up to measure the wave speed through sand that has a static pressure applied to it, as is done with the pressure plate in the penetration experiments.

4.4 Numerical Simulations

A numerical model was created using EMU peridynamic code to model the penetration event. The initial simulations were on a smaller scale than the penetration experiments, however they did show many of the same phenomenon observed in experiments. These phenomenon include the creation of force chains, a compaction wave, grain fracture and grains that “ride along” with the dart. It would be advantageous to make the model more accurate by modeling the entire tank of sand. It may also be important to add a model for grain on grain friction into the simulations. Another possible addition to the model would be to add water, and model the interactions of wet sand. This would be a logical next step if wet sand penetration experiments are conducted.

REFERENCES

1. Allen, William A., Earle B. Mayfield, and Harvey L. Morrison. “Dynamics of a Projectile Penetrating Sand.” *Journal of Applied Physics* 28, no. 3 (1957): 370. doi:10.1063/1.1722750.
2. Allen, William A., Earle B. Mayfield, and Harvey L. Morrison. “Dynamics of a Projectile Penetrating Sand. Part II.” *Journal of Applied Physics* 28, no. 11 (1957): 1331. doi:10.1063/1.1722645
3. Liu, Chu-heng, and Sidney Nagel. “Sound in a Granular Material: Disorder and Nonlinearity.” *Physical Review B* 48, no. 21 (December 1993): 15646–15650. doi:10.1103/PhysRevB.48.15646.
4. Savvateev, A. F., A. V. Budin, V. A. Kolikov, and Ph G. Rutberg. “High-speed Penetration into Sand.” *International Journal of Impact Engineering* 26, no. 1 (2001): 675–681.
5. Goldman, Daniel I. “Scaling and Dynamics of Sphere and Disk Impact into Granular Media.” *Physical Review E* 77, no. 2 (February 2008). doi:10.1103/PhysRevE.77.021308.
6. Cooper, William L., and Bradley A. Breaux. “Grain Fracture in Rapid Particulate Media Deformation and a Particulate Media Research Roadmap from the PMEE Workshops.” *International Journal of Fracture* 162, no. 1–2 (March 26, 2010): 137–150. doi:10.1007/s10704-010-9467-8.
7. Umbanhowar, Paul, and Daniel Goldman. “Granular Impact and the Critical Packing State.” *Physical Review E* 82, no. 1 (July 2010). doi:10.1103/PhysRevE.82.010301.
8. Omidvar, Mehdi, Magued Iskander, and Stephan Bless. “Stress-strain Behavior of Sand at High Strain Rates.” *International Journal of Impact Engineering* 49 (November 2012): 192–213. doi:10.1016/j.ijimpeng.2012.03.004.
9. Marston, J. O., I. U. Vakarelski, and S. T. Thoroddsen. “Sphere Impact and Penetration into Wet Sand.” *Physical Review E* 86, no. 2 (August 2012). doi:10.1103/PhysRevE.86.020301.
10. Martin, B.E., Md. E. Kabir, and W. Chen. “Undrained High-pressure and High Strain-rate Response of Dry Sand Under Triaxial Loading.” *International Journal of Impact Engineering* 54 (April 2013): 51–63. doi:10.1016/j.ijimpeng.2012.10.008.
11. Pica Ciamarra, Massimo, Antonio Lara, Andrew Lee, Daniel Goldman, Inna Vishik, and Harry Swinney. “Dynamics of Drag and Force Distributions for Projectile Impact in a Granular Medium.” *Physical Review Letters* 92, no. 19 (May 2004). doi:10.1103/PhysRevLett.92.194301.
12. Borg, J.P., and T.J. Vogler. “Mesoscale Simulations of a Dart Penetrating Sand.” *International Journal of Impact Engineering* 35, no. 12 (December 2008): 1435–1440. doi:10.1016/j.ijimpeng.2008.07.064.
13. Dwivedi, S. K., R. D. Teeter, C. W. Felice, and Y. M. Gupta. “Two Dimensional Mesoscale Simulations of Projectile Instability During Penetration in Dry Sand.” *Journal of Applied Physics* 104, no. 8 (2008): 083502. doi:10.1063/1.2999391.
14. Collins, A.L., J.W. Addiss, S.M. Walley, K. Promratana, F. Bobaru, W.G. Proud, and D.M. Williamson. “The Effect of Rod Nose Shape on the Internal Flow Fields During the

Ballistic Penetration of Sand." *International Journal of Impact Engineering* 38, no. 12 (December 2011): 951–963. doi:10.1016/j.ijimpeng.2011.08.002.

15. Borg, J.P., M.P. Morrissey, C.A. Perich, T.J. Vogler, and L.C. Chhabildas. "In Situ Velocity and Stress Characterization of a Projectile Penetrating a Sand Target: Experimental Measurements and Continuum Simulations." *International Journal of Impact Engineering* 51 (January 2013): 23–35. doi:10.1016/j.ijimpeng.2012.07.009.
16. "Nobuhito Mori and Kuang-An Chang (2003) "Introduction to MPIV", user reference manual, 14p.
17. "EMU - About EMU." Accessed May 3, 2013. http://www.sandia.gov/emu/emu.htm.
18. Kimberley, Ramesh and Barnouin, Visualization of the failure of quartz under quasi-static and dynamic compression, J. GEOPHY R., 2010
19. "ASM Material Data Sheet." Accessed May 5, 2013. http://asm.matweb.com/search/SpecificMaterial.asp?bassnum=MA6061t6.
20. Mark, James E. *Physical Properties of Polymers Handbook*. New York, NY: Springer, 2007.

APPENDICES

A.1. Oscilloscope Settings

	Velocity Block	Pressure Gauges
Vertical divisions	500 mV	20 mV
Horizontal Divisions	50 µs	200 µs
Horizontal Offset	125 µs	750 µs
Trigger Type	Edge	Edge
Trigger Source	Channel 1	Photron Camera
Trigger Slope	Falling	Rising
Trigger Threshold	450 mV	2 V
HF Reject	On	Off
Noise Reject	Off	Off

A.2. Sabot Dimensions

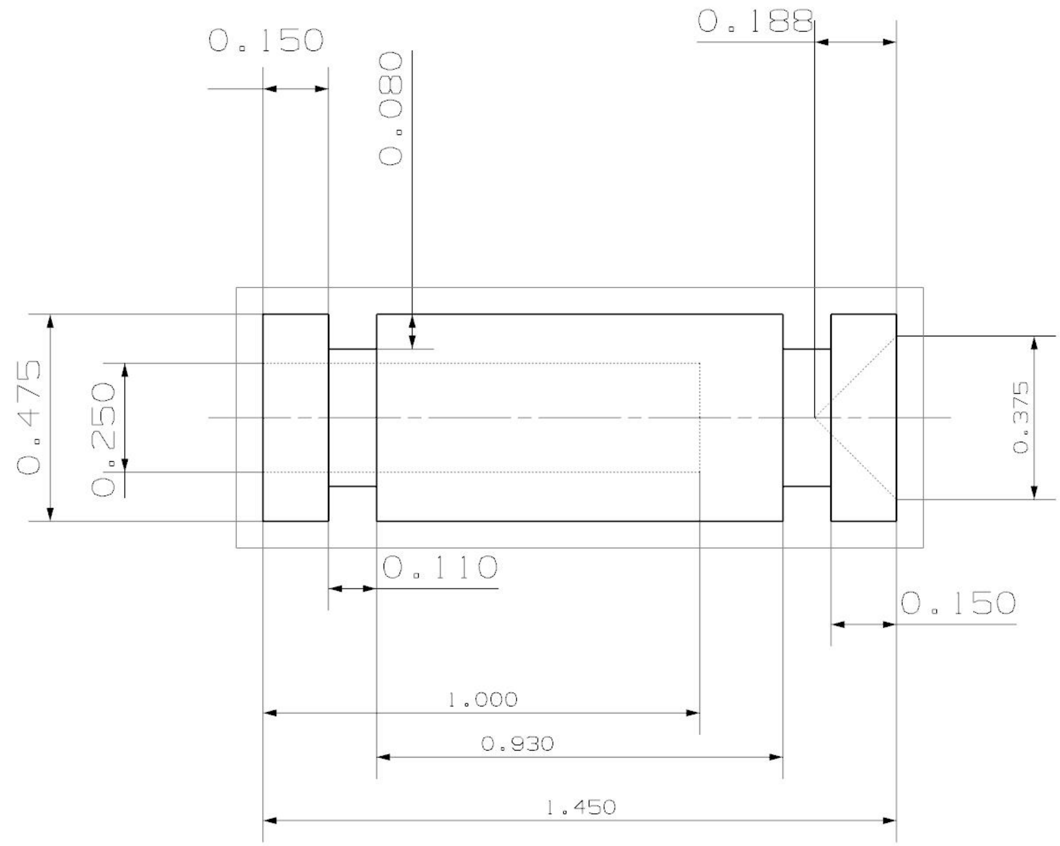

All dimensions are in inches, and dimensions with large text size are important dimensions for producing a successful shot.